All room-temperature synthesis, N$_2$ photofixation and reactivation over 2D cobalt oxides

Haijiao Lu [a,1], Yi-Ming Zhao [b,1], Sandra Elizabeth Saji [a,1], Xinmao Yin [c,d], Ary Wibowo [e], Chi Sin Tang [d,f], Shibo Xi [d,g], Pengfei Cao [h,*], Mike Tebyetekerwa [i], Borui Liu [a,j], Marc Heggen [h], Rafal E. Dunin-Borkowski [h], Antonio Tricoli [a,j], Andrew T.S. Wee [d], Hieu T. Nguyen [e], Qing-Bo Yan [b,*], Zongyou Yin [a,*]

[a] Research School of Chemistry, Australian National University, Canberra, Australian Capital Territory 2601, Australia
[b] Center of Materials Science and Optoelectronics Engineering, College of Materials Science and Optoelectronic Technology, University of Chinese Academy of Sciences, Beijing 100049, China
[c] Shanghai Key Laboratory of High Temperature Superconductors, Physics Department, Shanghai University, Shanghai 200444, China
[d] Department of Physics, Faculty of Science, National University of Singapore, 117542, Singapore
[e] School of Engineering, Australian National University, Canberra, Australian Capital Territory 2601, Australia
[f] Institute of Materials Research and Engineering, A*STAR, Agency for Science, Technology and Research, 138634, Singapore
[g] Institute of Chemical and Engineering Sciences, A*STAR, 138634, Singapore
[h] Ernst Ruska-Centre for Microscopy and Spectroscopy with Electrons and Peter Grünberg Institute "Forschungszentrum Jülich GmbH", Jülich 52425, Germany
[i] School of Chemical Engineering, The University of Queensland, St Lucia, Brisbane 4072, Australia
[j] Faculty of Engineering, University of Sydney, Darlington, New South Wales 2008, Australia

ARTICLE INFO

ABSTRACT

Ammonia is an indispensable chemical to the ecosystem and human beings. Storing solar energy in N-H bonds in NH$_3$ is a promising sustainable alternative to the energy-consuming Haber Bosch process. However, nitrogen photofixation with this strategy still suffers from several unsolved issues, such as high-energy consumption with carbon footprint, short lifetime of photocatalysts, and nitrogen contamination in redox reactions. In this study, a room-temperature strategy is developed to two-dimensionally assemble the diminutive CoO-Co$_3$O$_4$ mixed-oxide composites on reduced graphene oxide. They proffer great surface area and deep-red-light absorbing defect states, which enable them to exhibit over 14 times higher photoactivity than template-free single components. The unveiled photoreaction-induced cation oxidation is reversely triggerable by photo-reactivating Co$_3$O$_4$ back to active CoO, with well-maintained photoactivity after six-cycles. All these room-temperature processes, from catalyst synthesis, nitrogen photofixation, to catalyst reactivation, offer facile way towards upscaling and hold great promise for practical zero-emission N$_2$ photofixation.

1. Introduction

Ammonia (NH$_3$) is a chemical of paramount importance to both the ecosystem and human beings, which is especially used for the synthesis of fertilizers and thus feeding life on Earth. Owing to large hydrogen capacity and high energy density, it has also attracted great interest in the emerging carbon-free hydrogen economy [1,2]. The production of NH$_3$ from the extremely abundant but stable nitrogen (N$_2$) has always been among the hottest research topics, bagging three Nobel Prizes in

Chemistry in 1918, 1931 and 2007 [3]. The Haber-Bosch process represents a gigantic scientific breakthrough that has profoundly changed the whole world by supplying more than 200 million tons of NH$_3$ per year [2]. However, the high temperature and pressure conditions, large energy and H$_2$ consumption, and substantial energy-related CO$_2$ emissions have also brought growing challenges. Therefore, sustainable synthesis of NH$_3$ by low energy-consuming processes has attracted keen interest from researchers. N$_2$ photofixation, i.e. photocatalytic nitrogen reduction reaction (NRR), has been recognized as a promising

technology for NH_3 production at ambient temperature and pressure driven by renewable solar energy [4,5]. Photocatalysis also has significant importance in the preparation of H_2 utilizing the power of sunlight. Researchers investigated various kinds of photocatalysts including heterostructures and defect engineered materials [6–8]. The photocatalytic H_2 generation are a promising way to mitigate the energy crisis and green-house effects.

The main focus of a photocatalytic process is to develop a photocatalyst to directly store solar energy in N-H bonds without the assistance of external bias (wired electrodes) or harsh electrolyte, for a sustainable and readily-scalable redox reaction process. Transition-metal species have long been discovered to bind N_2 at low temperatures due to their favorable combination of unoccupied and occupied d orbitals [9–11], which possess suitable energy and symmetry to synergically accept electrons from N_2 and back donate to N_2. The back-donation process is crucial to effectively bind and activate N_2, as it can not only weaken the N≡N bond but also strengthen the metal-N bond [12]. The growth in demand of transition metal Co, for use in a variety of low carbon energy production and storage technologies, is expected to be as high as 585% in 2050 compared with that in 2017, only second to lithium among different kinds of minerals [13]. Cobalt oxide photocatalysts are favorable candidates due to their high catalytic activity, low cost and potential practicality [14–16].

With the upward shift of band edges, CoO has proved to be an efficient photocatalyst for overall water splitting under visible light with a solar-to-hydrogen efficiency of around 5% [17]. CoO was also predicted to be a favorable catalyst for NRR by density functional theory (DFT) calculations, confirmed by efficient electrocatalytic NRR on CoO quantum dots/reduced graphene oxide (RGO) [18]. However, the poor photostability of CoO, induced by half oxidation reaction, urgently needs to be solved to enable its application in photocatalysis [19,20]. Co_3O_4 is more stable than CoO under light illumination, has been found to be active in water oxidation [21–23] and has also been reported as Co_3O_4/RGO for electrocatalytic NRR [24]. The main limitation of pure Co_3O_4 as a photocatalyst without external bias is that it prefers oxidation reaction to reduction reaction and its separation of photogenerated electron-hole pairs is slow [21,25]. In this work, RGO-templated two-dimensionally (2D) arranged CoO-Co_3O_4 mixed-oxide (CoO dominated) composites were synthesized through a simple and facile route at room temperature, which exhibited remarkably enhanced photostability compared with the pure CoO as previously reported. This is attributed to the synergistically assigned two half reactions with reduction and oxidation spatially separated at CoO and Co_3O_4, respectively. During the extended photoreaction, the unveiled self-oxidation of CoO to Co_3O_4 was probably induced by the released O_2 from water oxidation. Impressively, this is readily reduceable/recyclable by photo-reactivating the non-active Co_3O_4 back to the active CoO at room temperature, with well-maintained photoactivity after six cycles of operation.

2. Experimental

2.1. Materials

Graphene oxide (300–500 nm, Suzhou Tanfeng Graphene Technology Co., Ltd.), $CoCl_2$•$6H_2O$ (≥ 98%, Sigma Aldrich), NaOH (≥ 98%, Chem-Supply), $NaBH_4$ (≥98%, Sigma Aldrich), methanol (≥ 99.9%, Sigma Aldrich), salicylic acid (≥ 99.0%, Sigma Aldrich), sodium citrate dihydrate (≥ 99.0%, Sigma Aldrich), sodium nitroprusside dihydrate (≥ 99.0%, Sigma Aldrich), sodium hypochlorite (reagent grade, available chlorine 10–15%, Sigma Aldrich) and phenol (≥99.5%, Sigma Aldrich) were used without further purification. N_2 gas (99.999%, Ultra High Purity Grade 5.0, BOC) or $^{15}N_2$ gas (98 atom % ^{15}N, Sigma Aldrich) was used as nitrogen source and deionized water (18.2 MΩ·cm) was used throughout the experiments.

2.2. Characterization

Powder X-ray diffraction (pXRD) patterns were collected by using a PANalytical Empyrean diffractometer with Cu-Kα radiation (λ = 1.54056 Å) operated at 40 kV, 40 mA and a scanning speed of 0.022255°/s. Scanning electron microscopy (SEM) was performed on a Zeiss UltraPlus FESEM at 3 kV. X-ray absorption near-edge structure (XANES) and X-ray absorption fine structure spectroscopy (EXAFS) data was obtained using linearly polarized X-ray absorption spectroscopy at the X-ray Absorption Fine structure for catalysis (XAFCA) beamline at the Singapore Synchrotron Light Source (SSLS), using a total electron yield (TEY) detection method. The incidence angle (90–θ) of X-rays is measured relative to the normal of the sample surface, and was varied by rotating the polar angle of the sample. The spectra were normalized to the integrated intensity spectra after subtracting an energy-independent background. High-resolution X-ray photoelectron spectroscopic (XPS) data were then taken under ultrahigh vacuum conditions at the Surface, Interface, and Nanostructure Science (SINS) beamline at the SSLS. This beamline is equipped with a VG/Scienta R4000 electron energy analyzer where the photon energy was calibrated using the Au 4 $f_{7/2}$ core level peak at 84.0 eV of a gold foil that is sputter-cleaned in electrical contact with the sample. The aberration-corrected (Cs corrector) high-resolution transmission electron microscopy (HRTEM) experiments were performed on an FEI Titan 80–300 microscope at 300 kV, which was equipped with a 2k × 2k Gatan UltraScan 1000 CCD camera. High-angle annular dark-field (HAADF) scanning transmission electron microscopy (STEM) imaging, energy-dispersive X-ray spectroscopy (EDS) mapping and electron energy-loss spectroscopy (EELS) analysis were conducted using a FEI Titan G2 80–200 microscopy at 200 kV, equipped with a Cs-probe corrector, four large-solid-angle symmetrical Si drift detectors, and Gantan dual EELS detector. Micro-Raman spectroscopy was measured on a Horiba Jobin-Yvon T64000 spectrometer system equipped with a 532 nm laser for excitation. UV-Vis diffuse reflectance spectroscopy (UV–vis DRS) was carried out on a PDA UV/Vis Lambda 465 Spectrophotometer (PerkinElmer). Nitrogen-adsorption isotherm surface area measurements were carried out with a Tristar II Surface Area Analyzer (Micromeritics). Mott-Schottky and Nyquist analyses were carried out using a PARSTAT 3000 electrochemical workstation (Princeton Applied Research). UV-Vis absorption spectroscopy was performed on a Cintra 2020 (GBC Scientific Equipment) spectrophotometer. Liquid chromatography-mass spectrometry (LC-MS) was carried out on an Orbitrap Elite™ Hybrid Ion Trap-Orbitrap Mass Spectrometer (Thermo Fisher) equipped with a C18 reversed phase high-performance liquid chromatography column (Thermo Fisher).

2.3. Synthesis

2.3.1. RGO/CoO/Co_3O_4

10 mg graphene oxide (GO) was added into 30 mL deionized water and the resulting suspension was sonicated (FX14, Unisonics) for 30 min to form a homogeneous black suspension. 3.66 mmol $CoCl_2$•$6H_2O$ (0.4759 g) was dissolved in deionized water to form a 10 mL solution. 1 mL $CoCl_2$ solution was added into GO suspension dropwise under stirring (Hei-Tec, Heidolph), and the resulting suspension was stirred for another 1 h. Each milliliter of the remaining 9 mL $CoCl_2$ solution was added following the same procedure. 2 M NaOH solution was added into the suspension dropwise under stirring until the pH reached 12. The resulting suspension was left stirring for 2 h. The solid was collected by centrifugation (5430, Eppendorf) and then dried in a vacuum oven (TVO-35, Thermoline L+M) overnight. 2 mL newly prepared 0.10 M $NaBH_4$ solution was added to the suspension of the dried solid in 10 mL water under stirring. After stirring for another 30 min, the final solid was centrifuged and dried in a vacuum oven for 4 h.

2.3.2. CoO/Co_3O_4

The synthesis of this composite is the same as above for RGO/CoO/

Co$_3$O$_4$, except that the GO template was removed.

2.3.3. CoO

CoCO$_3$ powder was calcined using a muffle furnace (YKY, CY Scientific Instrument) at 300 °C for 3 h with a ramping rate of 5 °C min^{-1} in Argon.

2.3.4. Co$_3$O$_4$

CoCO$_3$ powder was calcined using a tube furnace (YKY, CY Scientific Instrument) at 300 °C for 3 h with a ramping rate of 5 °C min^{-1} in Air.

2.3.5. RGO

25 mg GO was added into 50 mL deionized water and the resulting suspension was sonicated (FX14, Unisonics) for 30 min to form a homogeneous black suspension. 5 mL newly prepared 0.10 M NaBH$_4$ solution was added to the suspension dropwise under stirring. After stirring for another 30 min, the solid was collected by drying in a vacuum oven overnight.

2.4. Photocatalysis experiments

Specified amount of the as-prepared photocatalyst was added into 6 mL deionized water in a quartz bottle tightly sealed by a septum and parafilm. The suspension was sonicated (B2500R-DTH Ultrasonic Cleaner, Branson) for 10 min and then degassed using nitrogen gas (99.999%, BOC) for 30 min under stirring in the dark. Under a N$_2$ flow of 20 mL min^{-1}, the suspension was illuminated by 300 W Xenon lamp source (PLS-SXE300D, Beijing Perfectlight) with AM 1.5 G filter for 2, 4, 6, 8, 10 h under stirring respectively. As depicted in Fig. S1, the gas from the quartz reaction bottle flowed through a tube into 3 mL 0.5 M H$_2$SO$_4$ solution in a glass bottle (named as bottle C).

The ammonia produced from photocatalytic conversion was fully absorbed/collected by both water in the quartz bottle and H$_2$SO$_4$ solution in the bottle C abovementioned. Clear solution was collected after the suspension in the quartz bottle going through a filter membrane (0.22 μm pore size). The yield of ammonia was measured using the indophenol blue method [26]. Briefly, 1.5 mL of the filtered solution was added into 1.5 mL 0.5 M H$_2$SO$_4$ solution in a glass bottle (named as bottle R). 150 μL of solution A (1.25 g salicylic acid and 1.25 g sodium citrate dissolved in 6.785 mL 2 M NaOH), 30 μL of solution B (0.1 g sodium nitroprusside dissolved in 10 mL deionized water) and 30 μL of solution C (550 μL sodium hypochlorite solution dissolved in 25 mL 2 M NaOH) were all added into both bottle C and bottle R as color indicators. Bottles C and R were then fastened onto a shaker (Multi Reax, Heidolph) and kept shaking for 1 h to form indophenol blue. After that, the amount of indophenol blue was determined using the absorbance at a wavelength of 700 nm using UV–vis spectrophotometer. Absolute calibration of the method was performed using ammonium chloride solutions of known concentrations as standards, and the concentrations of ammonia in the solutions of both bottle R and bottle C were calculated using the pre-established calibration curve. The overall yield of ammonia was the sum of the value of bottle C and four times of that of bottle R.

2.5. Isotope labeling experiments

The isotope labeling experiments were carried out following the previously published procedure [27]. 6 mg of the as-prepared photocatalyst was added into 6 mL deionized water in a quartz bottle tightly sealed by a septum and parafilm. The suspension was sonicated (B2500R-DTH Ultrasonic Cleaner, Branson) for 10 min and then degassed using ^{15}N$_2$ (> 98 atom %, Sigma-Aldrich) and ^{14}N$_2$ (99.999%, BOC), respectively, for 30 min under stirring in the dark. Then, the two quartz bottle reactors were tightly sealed without further nitrogen supply or connection with glass bottle C. The suspensions in the two reactors were illuminated by 300 W Xenon lamp source (Mircosolar300, Beijing Perfectlight) without filter at the same conditions for 24 h under

stirring, respectively. The clear solutions were collected and further treated following the procedures in 'Photocatalysis experiments' except that 150 μL of phenol solution (1.25 g phenol dissolved in 6.785 mL 2 M NaOH) instead of solution A was used as an indicator. After shaking for 1 h, the solutions were analyzed by LC-MS.

2.6. Reactivation experiments

For reactivation experiments, after each cycle of photocatalytic NRR experiment (8 h illumination), the suspension in the quartz bottle was centrifuged and the solids were dried in a vacuum oven for 4 h. 15 mg dried solid was added into 3 mL methanol in a quartz bottle tightly sealed by a septum and parafilm. Then, the suspension was sonicated (B2500R-DTH, Branson) for 10 min and then degassed using Argon for 30 min under stirring. After that, the suspension was illuminated by 300 W Xenon lamp source (PLS-SXE300D, Beijing Perfectlight) without filter for 2 h under stirring. The solid was collected by centrifugation and dried in a vacuum oven for 4 h. After that, the photocatalyst was reused for the next cycle and six cycles of photocatalytic NRR experiments were conducted.

2.7. Time-resolve photoluminescence (TRPL) measurements

TRPL curves were captured at room temperature using an Horiba iHR 320 mm spectrophotometer equipped with a compact single-photon silicon detector (PPD-900, detection range between 350 and 920 nm). A 485-nm picosecond pulse laser (Horiba DeltaDiode) was used as an excitation source with a pulse width of 80 ps. The laser light was focused on the CoO, Co$_3$O$_4$ and RGO/CoO/Co$_3$O$_4$ samples through an Olympus BX53 microscope equipped with a 50x objective lens and an X-Y micropositioner. All measurements were done with a 16.6 MHz repetition rate. The lifetimes were calculated by fitting the decay curves with a biexponential decay function.

2.8. Ab initio calculations

All the geometric structure and energy were calculated by means of Vienna *Ab initio* Simulation Package (VASP) [28] based on DFT with projected augmented wave (PAW) method [29]. The exchange and correlation interactions between electrons are described by the generalized gradient approximation (GGA) with the Perdew-Burke-Ernzerhof (PBE) functional [30]. The Coulomb repulsion U is set as 3.7 eV for Co 3d orbital [31]. The DFT-D3 method is used to take the van der Waals interaction into consideration [32]. The geometric structures have been fully optimized until the force on each atom is smaller than 0.02 eV/Å and the convergence criterion for energy is 10^{-5} eV. The entropy and zero point energy are obtained from the vibration frequencies over Γ point for the correction of Gibbs free energy [33].

3. Results and discussion

3.1. Catalyst characterizations

As shown in Fig. 1a, the fresh photocatalyst (PC-fresh) showed signals corresponding to Co$_3$O$_4$ (JCPDS card PDF file no. 42–1467) and CoO (JCPDS card PDF file no. 48–1719), suggesting crystallization even under the room-temperature synthesis process. Co K-edge XANES was measured to reveal the fine structure of PC-fresh. As the inset of Fig. 1b shows, the blue line of PC-fresh in the XANES spectra was between that of CoO and Co$_3$O$_4$, suggesting the co-existence of CoO and Co$_3$O$_4$. The simulation results of Fourier transformed extended X-ray absorption fine structure (FT-EXAFS) reveal that PC-fresh contained 58.9% CoO and 41.1% Co$_3$O$_4$ with oxygen vacancies (V$_O$). The Co 2p$_{3/2}$ XPS spectrum (Fig. 1c) also revealed that PC-fresh contained both Co^{3+} (~780.3 eV) and Co^{2+} (~781.3 eV) [34,35]. HRTEM image (Fig. 1d) shows that the spacing between lattice fringes with an angle of 60° is 0.285 nm, which
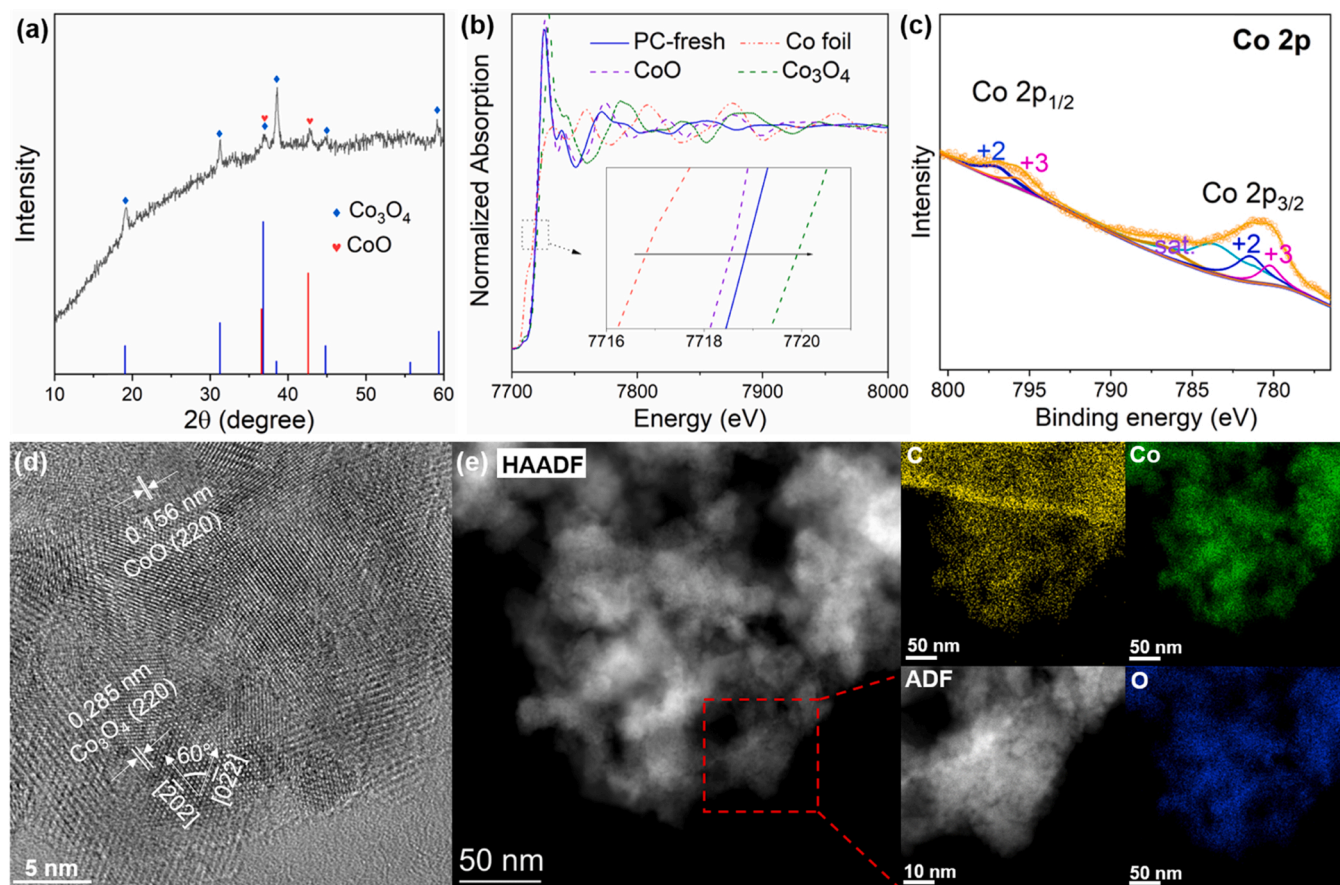
Fig. 1. (a) pXRD, (b) XANES spectra, (c) XPS, (d) HRTEM and (e) HAADF and ADF/EDS (C, Co and O) mapping of the fresh photocatalyst.

is consistent with the (202) and (022) planes of cubic Co_3O_4 [36], and the lattice fringes corresponding to the (220) plane of the rock salt cubic CoO (D-spacing 0.156 nm) [37] can also be observed. In Fig. S2A, the SEM image of PC-fresh shows two-dimensionally arranged nanoparticles on nanosheets with a lateral size of 200–300 nm. Combining with the results of HRTEM in Fig. 1d, the nanoparticles and nanosheets can thus be corresponded to cobalt oxides and substrate/template, respectively. HAADF/EDS mapping in Fig. 1e displays the consistent overlapping of C element from substrate/template (excluding the lacey carbon support film from TEM grid) with Co and O elements from cobalt oxides, which were discerned to be ~ 2–8 nm in size. Note here, such fine particle size of cobalt oxides on RGO is not discernable by the SEM image (Fig. S2A). Furthermore, Raman spectra (Fig. S3) further verified that the substrate/template exhibited well-referred D band (1352 cm^{-1}) and G band (1598 cm^{-1}) corresponding to graphene-like structure. The I_D/I_G ratio of PC-fresh was 1.26, which was obviously larger than that of the GO precursor (1.15) and nearly identical as RGO (1.28). The Raman results suggest that the substrate/template for cobalt oxide within PC-fresh was RGO, which was reduced from the GO precursor by $NaBH_4$ during synthesis [38]. Therefore, these characterizations provide clear evidence that cobalt oxide (CoO and Co_3O_4) particles were well grown onto the RGO substrate/template in the PC-fresh.

3.2. NRR performance

The performance of the prepared catalysts was evaluated for photocatalytic NRR. As shown in Fig. 2a, the prepared photocatalyst, PC-fresh (RGO/CoO/Co_3O_4) possessed remarkably enhanced photocatalytic activity compared with the individual components CoO and Co_3O_4, and also the CoO/Co_3O_4 composite. The ammonia evolution rate at the ambient conditions is 89.1 μmol g^{-1} h^{-1} for PC-fresh, while those

for CoO, Co_3O_4 and CoO/Co_3O_4 are only 6.0 μmol g^{-1} h^{-1}, 5.5 μmol g^{-1} h^{-1} and 25.9 μmol g^{-1} h^{-1}, respectively. The background performance from the template of RGO is also presented for comparison, where its ammonia evolution rate is 4.0 μmol g^{-1} h^{-1}, negligible to that from PC-fresh sample. The reasons for the much higher performance from PC-fresh, ~ 14 times higher than that of CoO and Co_3O_4, will be investigated and discussed through the following different characterizations and theoretical calculations. First, SEM images in Fig. S2B, S2C and S2D show that the particle sizes of Co_3O_4, CoO and CoO/Co_3O_4 were around 30–100 nm, obviously larger than the size of cobalt oxides grown on the template of RGO (about 2–8 nm), based on the STEM characterization (Fig. 1e, S11A, S12, S14). This is significant as it indicates that the RGO, as a template, can effectively promote the nucleation and growth of diminutive cobalt oxide nanoparticles with the 2D arrangement. Correspondingly, as shown in Fig. S5, the specific surface area of RGO/CoO/Co_3O_4 was measured to be 317 m^2 g^{-1}, remarkably larger than that of CoO (57 m^2 g^{-1}), Co_3O_4 (111 m^2 g^{-1}), and of Co_3O_4/CoO (93 m^2 g^{-1}). The above results verify that by using RGO as the template for the synthesis of cobalt oxides, the particles size of cobalt oxides decreases and hence surface area increases. These greatly benefit light harvesting and N_2 molecules adsorption, enhancing the performance of RGO/CoO/Co_3O_4, as compared to that of CoO, Co_3O_4 and Co_3O_4/CoO (Fig. 2a). Note, from single components (CoO and Co_3O_4) to the composite (RGO/CoO/Co_3O_4), the surface areas only increase by several times, but the performance rises by ~ 14 times. This implies that the performance depends not only on catalyst-light-/-N_2 interaction, but also on the catalyst's own properties associated with charge carrier transportation and reaction path, which will be further discovered together with the mechanistic study by combination with theoretical calculations below. It is worth noting here that compared with the short lifetime (1 h) of pure CoO [19,39], PC-fresh RGO/CoO/Co_3O_4 photocatalyst in this work

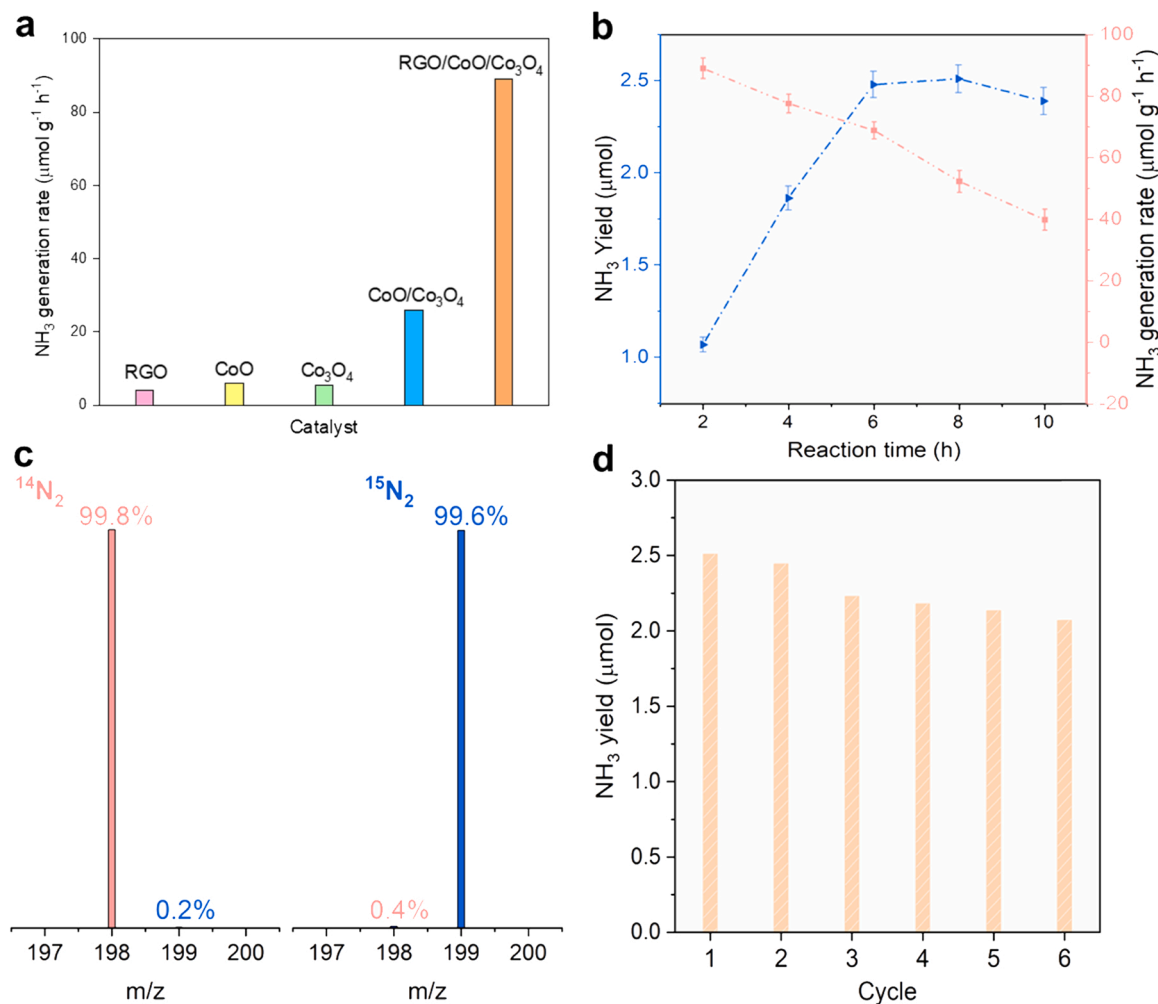**Fig. 2.** (a) NH_3 average generation rates by different catalysts, (b) NH_3 yields and average generation rates by 1 mg mL^{-1} $RGO/CoO/Co_3O_4$ under different illumination lengths of time for photoreaction, (c) LC-MS charts of indophenols in the solutions obtained by the reaction with $^{14}N_2$ and $^{15}N_2$, respectively, (d) NH_3 average generation rates in 6 cycles using 1 mg mL^{-1} $RGO/CoO/Co_3O_4$ for NRR, where 1 h UV light reactivation was applied to the photocatalyst after each cycle of 8-hour photoreaction.

exhibited a remarkably prolonged photocatalytic lifetime up to 8 h (Fig. 2b) under light irradiation. A decrease of total NH_3 yield after 8 h was most likely due to ammonia produced in the early 8 h being pushed/carried out with water without being collected by the continuous N_2 flow.

3.3. Isotope labeling results

It has been widely realized that NH_3 contamination from various sources, such as the catalyst, air, reaction vessels, and even human breath, has substantial influence on the reliability and reproductivity of NRR results, due to the small scale formation of ammonia product [40]. To verify N_2 gas as the source of NH_3 in this work, photocatalytic NRR with isotope-labeled $^{15}N_2$ gas was carried out parallel to the regular N_2 ($^{14}N_2$) gas NRR under identical reaction conditions detailedly described in the Supporting Information. As shown in Fig. 2c, the solutions obtained by the reaction with $^{15}N_2$ gas showed extremely high relative intensity (99.6%) of indophenol anion at m/z 199 with a negligible 0.4% of ^{14}N indophenol anion at m/z 198, while that of $^{14}N_2$ gas showed 99.8% of indophenol anion at m/z 198% and 0.2% at m/z 199 [41]. The results confirmed that contamination was successfully avoided and nitrogen gas was the only source of N element to form NH_3 in the photocatalytic system of this study. As shown in Fig. 2d, the average NH_3 generation rates decrease gradually in the consecutive six cycles under

the same reactivation time, i.e. 1 h by UV light. However, the NH_3 generation rate in the 6th cycle can still be attained as high as 82% of the 1st cycle, which is realized simply by 1 h UV light reactivation at room temperature.

3.4. Cation oxidation and the reactivation

Earlier reports have revealed that CoO suffers from poor stability due to the carrier recombination-induced thermal oxidation to accelerate the relocation of Co^{2+} cations and O^{2-} anions to form Co_3O_4 ultimately [19, 20]. In this work, the NRR-induced composition change of photocatalysts and the reactivation processes were investigated to understand the composition-performance relationships. As indicated by pXRD patterns, XANES spectra, XPS spectra and HRTEM (Fig. 3), CoO in the photocatalyst was gradually oxidized into Co_3O_4 during photocatalytic NRR. The cobalt oxide species of the used photocatalyst after one cycle (8 h) photoreaction, i.e. PC-1st-used in Fig. 3, were confirmed to be Co_3O_4 with oxygen vacancies by the simulation results of FT-EXAFS. That indicates, during 8 h NRR, the compositions of Co-based species were changing from the mixture of Co_3O_4 and CoO to almost only Co_3O_4 after CoO had been eventually oxidized/transformed to Co_3O_4. It is worth noting here that the photocatalytic activity from the PC-1st-used photocatalyst was significantly lower than that from the fresh photocatalyst, i.e. PC-fresh (Fig. 2b).
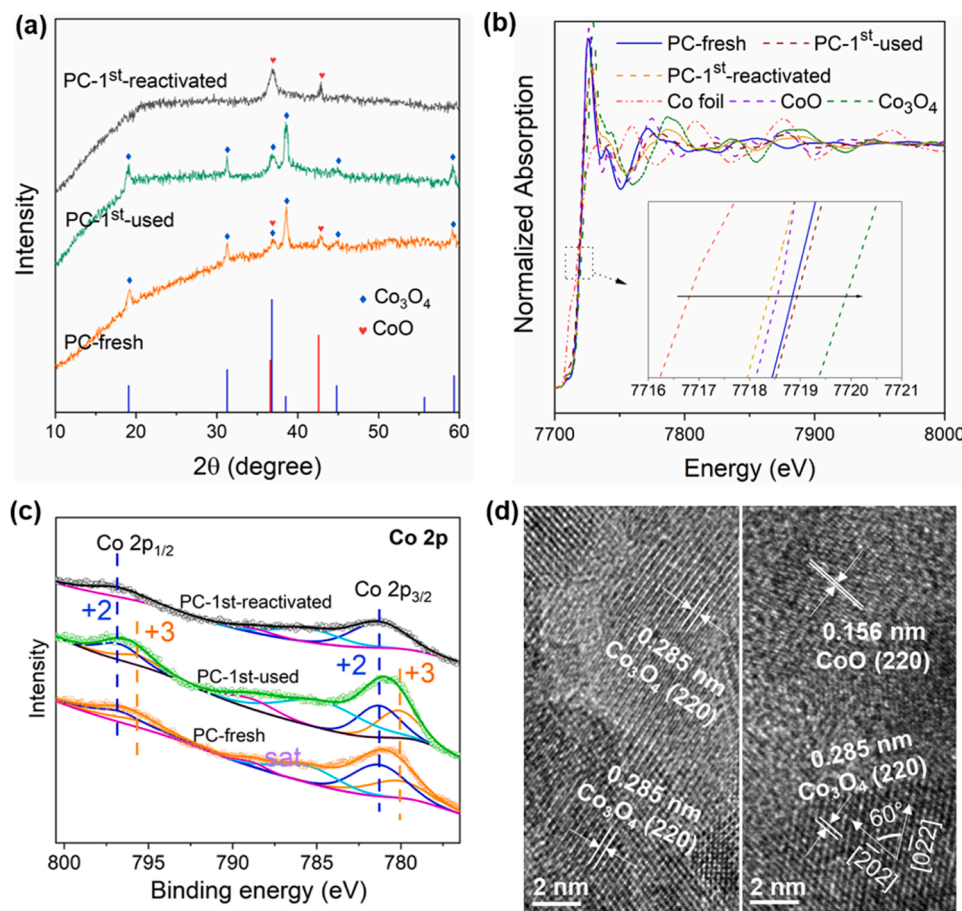
Fig. 3. (a) pXRD, (b) XANES spectra, (c) XPS spectra of freshly prepared photocatalyst (PC-fresh), used photocatalyst after 1st cycle (PC-1st-used) and reactivated photocatalyst after 1st cycle (PC-1st-reactivated) and (d) HRTEM of PC-1st-used (left) and PC-1st-reactivated (right).

In order to recover the used photocatalyst, it was then reactivated, i. e. reduction of Co_3O_4, by 1 h UV (optimized) light irradiation in methanol at room temperature (Fig. S8B). FT-EXAFS simulation based on the XANES spectra in Fig. 3b indicates that the cobalt oxide species in the reactivated photocatalysts, i.e. PC-1st-reactivated in Fig. 3, were 93.3% CoO and 6.7% Co_3O_4, suggesting that most of Co_3O_4 was converted back to CoO after reactivation. HRTEM (Fig. 3d right) captured the characteristic (220) plane of CoO along with the (202) and (022) planes of cubic Co_3O_4 in the reactivated photocatalyst, further confirming the co-existence of CoO and Co_3O_4. Due to the dominant content of CoO and low content of Co_3O_4 within the reactivated photocatalysts, it can be understood that the signals of Co_3O_4 in the reactivated photocatalysts were not detected by pXRD (Fig. 3a) and XPS (Fig. 3c). Again, in the used photocatalyst, only Co_3O_4 component was observed in HRTEM (Fig. 3d) left. This shows a good agreement with the results of EELS analysis. As shown in Figs. S10G, S11G and S13G, the volumetric atom density of Co on fresh, used and reactivated photocatalysts were calculated based on the EELS results. The volumetric atom density of Co on fresh catalyst is low, which became higher after photocatalytic NRR on the used catalyst. It indicates that the composition transformed from CoO to Co_3O_4 after the reaction. After reactivation by UV light irradiation in methanol at room temperature, most parts show a lower volumetric atom density of Co, implying that most of Co_3O_4 was converted back to CoO. To continue the studies on catalyst's performance recovery and endurance, the reactivated photocatalysts were then used for the next cycle of photocatalytic NRR (Fig. 2b). With the gradual oxidation of CoO to Co_3O_4 in the composite, the photocatalytic activity gradually decreased until reactivated by UV light before the subsequent cycle.

From the above unveiled composition-performance relationship,

more Co_3O_4 component in the composites led to the poorer performance in NRR, and in sharp contrast, more CoO favored NRR. As known, an NRR with photocatalysts suspended in pure water needs photogenerated electrons and hydrogen resource, i.e. protons (H^+) released from water oxidation reaction (OER) driven by photogenerated holes. Compared with 4-holes involved OER, 6-electrons reliant NRR is more challenging and is further affected by several other factors: the well-known low solubility of N_2 in H_2O, and competition with hydrogen evolution reaction; and the unknown catalyst's surface dependent N_2 adsorption-to-reaction path, and catalyst's electronic structure determined charge carrier transport behavior.

Therefore, the following mechanistic study on composite's CoO component reliant photoactivity will mainly focus on NRR, rather than OER. Note here, several considerations led us to exclude RGO's effect on NRR from the composite. First, RGO was mainly used as the template to anchor diminutive cobalt oxides particles with a nearly full coverage on the surface of RGO (Fig. 1e, S10A, S11A, S13A), leaving its very low exposure to the surface redox reactions. Second, our experimental results confirmed that RGO itself has negligible NRR performance compared with the composite (Fig. 2a). Third, theoretical calculation also indicates that there exists large barrier in NRR from RGO (Fig. S26-S27). It is worth noting here that the performance enhancement from CoO/Co_3O_4 to PC-fresh (RGO/CoO/Co_3O_4) is mainly attributed to the surface area increase induced by the much smaller size of cobalt oxide particles. Subsequently, further experiments related to the physical properties of cobalt oxides in the composite were carried out to help understand the underlying mechanism of the photoreaction.

3.5. Electronic structures

As the electronic structures of photocatalysts have significant impact on photocatalytic performance, the band edge (conduction band minimum, CBM; and valence band maximum, VBM) positions of CoO and Co_3O_4 were determined from the flat-band potentials in Mott-Schottky plots (Fig. S4) [42]. The energy bandgaps (E_g) of CoO and Co_3O_4, obtained from the UV-Vis absorption spectra, are $\sim$ 2.6 eV and $\sim$ 2.1 eV, respectively (Fig. 4b), which are consistent with previously reported papers [43,44]. Note here, as presented above, the diameter of CoO and Co_3O_4 particle in the composite is only about 2–8 nm, much smaller than the sole CoO and Co_3O_4 component particles of about 30–100 nm. It is well known that when a semiconductor's dimension goes down to less than 10 nm, its bandgap E_g increases as a blueshift is induced by the quantum size effect. Such blueshift scenario was observed from the obtained E_g of the PC-fresh, PC-1st-reactivated and PC-2nd-reactivated samples, which are all CoO dominated and consistently show a main peak at $\sim$ 2.9 eV (Fig. S6B). We also calculated the quantum confinement effect based on the DFT calculated band structures of CoO and Co_3O_4 as shown in Fig. S15 [45]. The CoO nanoparticles exhibit a 2.61 eV E_g, which is 0.23 eV larger than the bulk CoO. The increased E_g of nanoparticles demonstrating the blueshift of optical absorption is reasonable. Interestingly, this peak closely overlaps with that from Co_3O_4 component since the PC-1st-used (Co_3O_4 dominated) also showed a similar E_g at about 2.9 eV (Fig. S6B). For Co_3O_4, the calculated

nanoparticle E_g increases by 0.37 eV compared to the bulk Co_3O_4. Such E_g increase of 0.37 eV from Co_3O_4 is larger than the 0.23 eV from CoO, which is consistent with the observed larger blueshift of optical absorption peak of Co_3O_4 component (2.1–2.9 eV) compared to CoO (2.6–2.9 eV).

Note, all the CoO-dominated samples exhibited broad light absorption up to deep red, a wavelength of $\sim$ 700 nm in UV-DRS spectra (Fig. S6A), with the corresponding smaller E_g of $\sim$ 1.8 eV after fitting with Tauc plot from PC-fresh (Fig. 4b) and PC-1st/2nd-reactivated samples (Fig. S6D); similarly, $\sim$ 2.1 eV E_g was obtained from PC-1st-used sample (Fig. S6C). These narrower-gap light absorption features are associated with the defect states in CoO and Co_3O_4, which may be related to the room temperature, i.e. heat-free, synthesis for the composite. As the RGO was fully covered by cobalt oxide fine particles, its own optical absorption feature, for example, the fitted absorption energy of $\sim$ 2.6 eV (Fig. S7), was screened and not observable from any of the composite samples (Fig. S6), which further supports the feasibility to exclude RGO's effect on NRR afore-mentioned. The final electronic band structures of CoO/Co_3O_4 in the composite were obtained based on that of the single components CoO and Co_3O_4 as shown in Fig. 5a.

Both the band edges, i.e. CBM and VBM, of the intrinsic CoO and Co_3O_4 semiconductors straddle the NRR potential (N_2/NH_3) and OER potential (H_2O/O_2). However, the defect energy levels (DELs) of both CoO and Co_3O_4, which sit within the energy gap but close to VBMs due to their p-type doping/behavior (Fig. 4), shift their oxidation potential
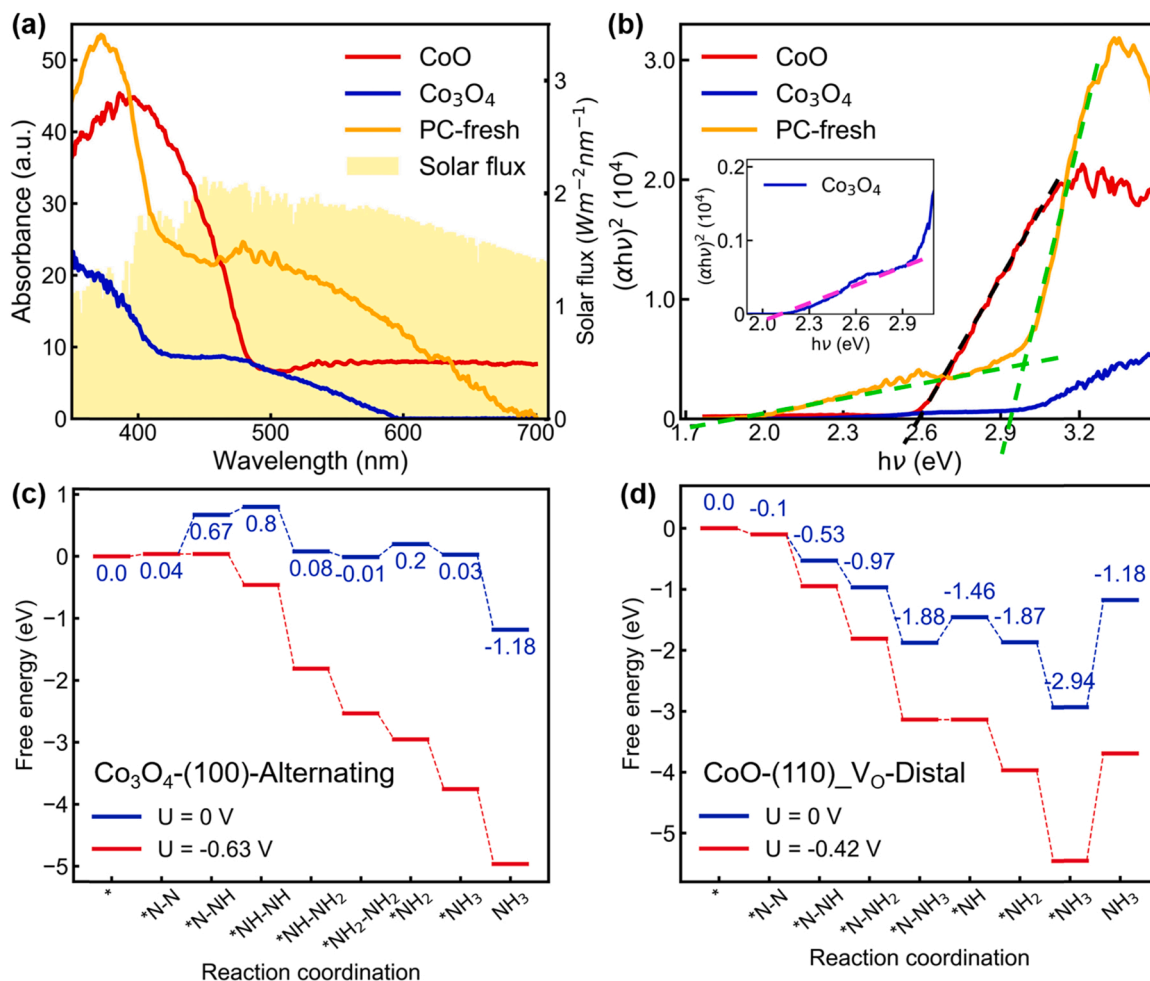

Fig. 4. (a) UV-Vis absorption spectra and (b) the based Tauc plot curves to obtain the energy bandgaps for CoO and Co_3O_4 single components, and those of CoO and Co_3O_4 in the composite. The variations of free energy along the (c) alternative path on the Co_3O_4-(100) surface and (d) distal path on the vacancy site of CoO-(110) surface with oxygen vacancy, were obtained from ab initio calculations. The blue and red paths are corresponding to the situations without potential and with certain potential U to overcome the energy barriers, respectively. The corresponding geometric configurations at all steps are shown in Fig. S24-S25.
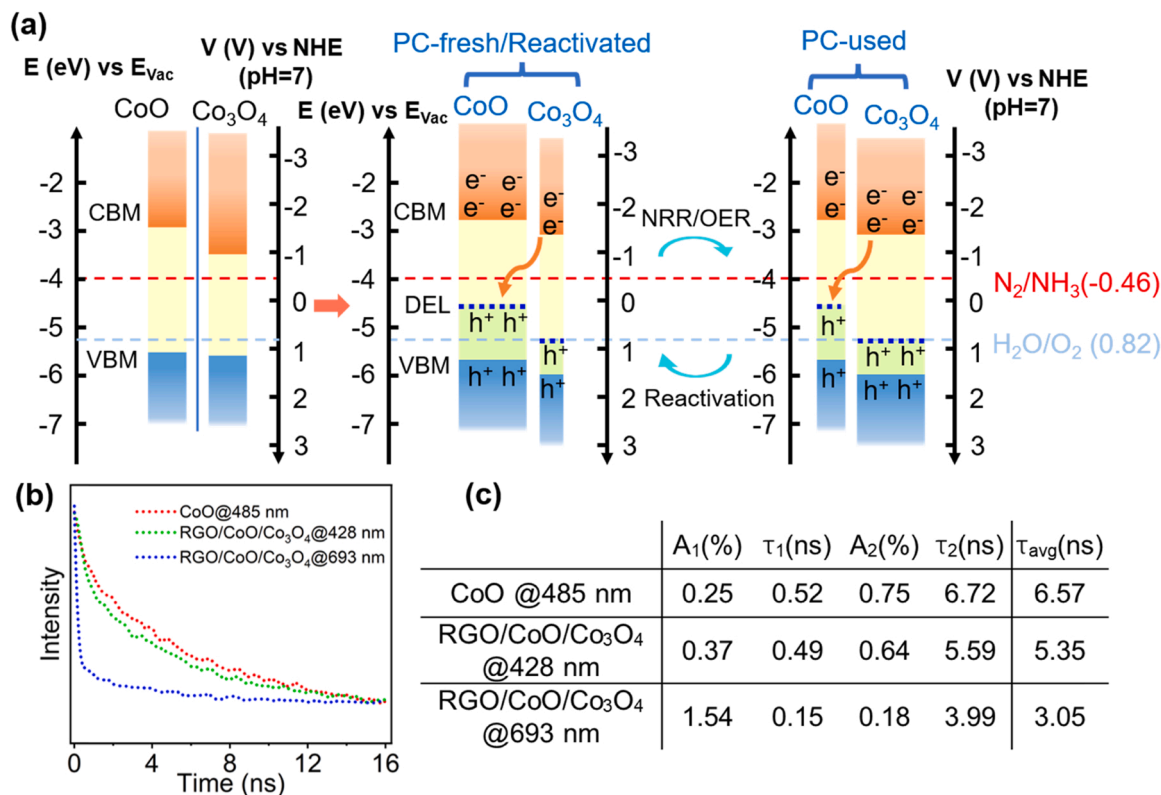
Fig. 5. (a) Electronic band structures for the recycled photocatalysts (from PC-fresh to PC-used to PC-reactived) deduced from the experiment results: first (left diagram), the fundamental electronic band structures for CoO and Co_3O_4 single components were built up based on their VBM values extracted from Mott-Schottky results in Fig. S4 and their energy bandgaps received in Fig. 4b. Second, the quantum effect induced E_g increases to ~ 2.9 eV after blueshift, where an equal upward and downward shift is applied to receive new CBM and VBM. Third, the V_O-related defect bandgaps for CoO and Co_3O_4 in the PC-fresh composite were received, where the V_O-related defect energy levels lie at 1.1 eV (= 2.9–1.8 eV) and 0.9 eV (= 2.9–2.0 eV) above the VBM level, respectively, negative to the VBMs of CoO and Co_3O_4, considering they both show p-type semiconductor nature (Fig. S4). E_{vac} and NHE represent the vacuum energy level and normal hydrogen electrode, respectively, which are energy references here. The red and blue dash lines indicate the nitrogen reduction potential (N_2/NH_3) and oxygen evolution potential ($H_2O/$O_2$) respectively. The charge transfer between CoO and Co_3O_4 through a direct Z-scheme mechanism is displayed. (b) Time-resolved photoluminescence decay curves, and (c) the fitted average carrier lifetime.

from the position of VBMs to DELs. As observed, DEL_{CoO} is much more negative to OER, not conducive to driving OER; while DEL_{Co3O4} almost overlaps with OER energy level, which may contribute to OER after the photogenerated holes accumulate there. This indicates that in order to fulfill the requirements on electronic structures for the above experimentally verified efficient NRR with CoO-dominated composite, the photogenerated electrons (e⁻) at CBM_{CoO} will engage more in half reduction reactions of NRR, but less in radiative recombination with the photogenerated holes (h⁺) at VBM_{CoO} or DEL_{CoO}. The holes required for the other half reaction (OER), to generate protons (H⁺) for NRR will rely on those at VBM_{Co3O4} and DEL_{Co3O4}. The h⁺/(VBM_{CoO}, DEL_{CoO}) will recombine with e⁻/CBM_{Co3O4} to release e⁻/CBM_{CoO} for NRR, and hence h⁺/(VBM_{Co3O4}, DEL_{Co3O4}) for OER. Based on these scenarios and the evidences from experimental results, a Z-scheme heterojunction is proposed to be formed between CoO-Co_3O_4 (Fig. 5a) [46]. In addition, the apparent quantum efficiency (AQE) for RGO/CoO/Co_3O_4 was measured under the same conditions, except that the monochromatic light (400 nm, 500 nm, 600 nm and 700 nm) was adopted as the light source, respectively (Fig. S9). The AQE was calculated by the following equation: [47].

$$AQE = N_e/N_p = 6*N_{NH3}/N_p = 6*v_{NH3}*N_A/(W*A*\lambda/h*c)$$

where N_e, N_p and N_{NH3} stand for the number of electrons reacted, incident photons and generated NH_3, respectively; v_{NH3}, N_A, W, A, λ, h, and c are the NH_3 generation rate, Avogadro's constant, incident light intensity, irradiation area, incident light wavelength, Planck constant, and speed of light, respectively. The highest efficiency for NRR is observed

when light of wavelength 400 nm is used, which excites the electrons of intrinsic CoO and Co_3O_4 ($E_g = ~ 2.9$ eV) to enhance NRR. 500 nm and 600 nm light can excite the electrons from the defect states of CoO and Co_3O_4, respectively, present at a band gap of 1.8 eV and 2 eV. Also, note that 500 nm shows a higher efficiency compared to 600 nm and a plausible mechanism for this could be that 500 nm has a higher energy to excite the electrons at defect states, thereby having more kinetic energy to take part in more nitrogen reduction processes. Finally, the 700 nm light with a very low energy is incapable of electron excitation which justifies the negligible quantum efficiency.

3.6. Theoretical understanding on NRR pathways

Furthermore, ab initio calculations were performed to reveal the adsorption of N_2 and NRR reaction path. We systematically studied the adsorption of N_2 on the low index ((100), (110) and (111)) crystal surfaces of CoO and Co_3O_4 and edge sites of RGO as shown in Fig. S16-S20. As listed in Table S1, the comparison of formation and adsorption energies for various adsorption configurations demonstrates that the pristine CoO-(100), CoO-(110) and Co_3O_4-(100) facets tend to adsorb N_2 molecule properly. Besides, the vacancy sites of CoO-(110) and Co_3O_4-(110) facets also exhibit moderate adsorption to N_2. The oxygen vacancy formation energy on CoO-(110) surface is 3.31 eV (Table S1) and the moderate defect formation energy indicate an adequate amount of oxygen vacancy to adsorb the N_2 molecule. The reaction paths on the sites of these five facets were further explored to evaluate the energy barrier along the pathway. Specifically, for the reduction of N_2 molecules in

end-on associative adsorption mode, two major reaction paths, i.e., distal pathway and alternative pathway [48], were considered (Fig. S21).

From the variation of specific free energy along the reaction path, the reaction barriers can be deduced, which directly affect the reaction rate of NRR. As shown in Fig. 4c, the highest reaction barrier on pristine Co_3O_4-(100) facets is 0.63 eV at the step of "N-NH". The NRR process on Co_3O_4-(100) facets can only proceed under a potential (U) of 0.63 eV. The energy difference between the CBM and NRR energy level will take effect as the potential which drive the photoexcited electrons to catalyze NRR [49,50]. The step of "N-NH" formation is the only endothermic step along the pathway. Once the NRR reaction passes the "N-NH" step, all the left steps are exothermic reactions which will proceed spontaneously from the thermodynamic view. As shown in Fig. 4d, the CoO-(110) surface with oxygen vacancies (CoO-(110)_V_O) reduces the NRR reaction barrier compared with the pristine CoO-(110) facets (Fig. S22). The highest barrier on CoO-(110)_V_O is 0.42 eV at the "NH" formation step, which is the only endothermic reaction step within the hydrogenation steps. Although the desorption of NH_3 meets a large energy barrier (about 2 eV) as shown in the last step, the solvation of ammonia in solution will decrease the free energy of the final product, which benefits stabilizing the desorbed ammonia and promoting the desorption of generated ammonia [49,51]. The energy barrier of CoO-(110)_V_O (0.42 eV) is lower than that of Co_3O_4-(100) facets (0.63 eV), indicating that the configuration of vacancy sites on CoO-(110) surface is more favorable for photocatalytic NRR. In contrast, as shown in Fig. S22-S23, the NRR barriers for pristine CoO-(100), CoO-(110) facets, and V_O site of Co_3O_4-(110) surface, are all larger than 1.0 eV, suggesting that they may have poor catalytic performance. The NRR barriers for RGO are even higher than 1.5 eV, as shown in Fig. S26-S27, indicating that RGO will not exhibit a high efficiency for photocatalytic NRR. Therefore, among various scenarios from CoO, Co_3O_4 and RGO, the configuration of V_O site on CoO-(110) surface exhibits the highest photocatalytic NRR efficiency. From this, it is reasonable to point out that the defects of V_O in CoO, not in Co_3O_4, of the composite dominate in N_2 adsorption and the subsequent reduction steps which promotes NRR.

3.7. Insights into photoactivity and reactivation

Following the above discussion, in the CoO/Co_3O_4 Z-scheme junction, the amount of the critical component CoO in the composite will dominate the NRR. As the photoreaction proceeds, the observed Co^{2+} to Co^{3+} cation oxidation with increasing Co_3O_4 amount in the composite could be associated with the accompanied oxidation process by the oxidative agents, such as photogenerated holes and O_2 from OER. The calculated projected density of states indicate that the electrons in CoO conduction band are capable to reduce N_2 and the holes in Co_3O_4 valence band are capable to oxidize H_2O as shown in Fig. S28 and S29, respectively. In contrary, the holes in CoO are not oxidative enough to catalyze OER and electrons in Co_3O_4 are not reductive enough to catalyze the NRR. The distribution of available electrons and holes also demonstrate that the redox reaction in CoO-Co_3O_4 system follows a Z-scheme pathway. When NRR diminished the CoO component after an 8 h reaction, as schematically presented in the band structure in Fig. 5a, the available reactivity sites from CoO will concurrently become fewer, which explains the decrease of NH_3 generation rate over one cycle (Fig. 2b).

If most of the photogenerated electrons at CBM_{CoO} migrate to CBM_{Co3O4}, and the holes at VBM_{Co3O4} and DEL_{Co3O4} transfer to the VBM_{CoO} and DEL_{CoO}, the reduction of N_2 and oxidation of H_2O will occur on Co_3O_4 and CoO, respectively. However, it contradicts with the higher reaction barrier of Co_3O_4 (Fig. 4c) and less favorable N_2 adsorption (Table S1) as well as the NH_3 generation rate decreased with the CoO oxidation over the reaction (Fig. 2b). What is more, as the CBM_{CoO} is more negative to CBM_{Co3O4}, the electrons on CBM_{CoO} are more reductive than those on CBM_{Co3O4}. The electrons transfer from CBM_{CoO} to CBM_{Co3O4} occurs in this CoO-Co_3O_4 system but the CBM to CBM routine is not a dominated pathway. The holes transfer from VBM_{Co3O4} (DEL-$_{Co3O4}$) to VBM_{CoO} (DEL$_{CoO}$) also occurs at a small possibility.

All of these factors discussed above demonstrate that the reduction of N_2 occurs on the surface of CoO. This further verifies that the CoO/Co_3O_4 configuration is a direct Z-scheme heterojunction, in which the electrons at CBM_{CoO} reduce the N_2 molecules and the holes at VBM_{Co3O4} and DEL_{Co3O4} oxidize the H_2O molecules, respectively. Impressively, the reduction of Co_3O_4 will trigger the backward transformation of the used/aged Co_3O_4 towards the active CoO (Fig. 5a), and hence the reactivity sites, i.e. the performance for photocatalytic NRR, were well reactivated in the subsequent cycles (Fig. 2d).

3.8. Carrier lifetime

In order to further verify charge carrier transport behavior in the active composites/catalysts dominated with CoO, the carrier lifetime for the PC-fresh composite and the control sample of single CoO component have been carried out. As known, TRPL decay is an important tool to gain insight about the lifetime of photoexcited excitons quantitatively. The experimental TRPL results for single components CoO and PC-fresh are shown in the Fig. 5b. A bi-functional exponential decay formula was used to fit the experimental TRPL data and average carrier lifetime (τ) could be determined from the following equation:[52].

$$\tau = \sum A_i \tau_i^2 / \sum A_i \tau_i$$

where A_i and τ_i are the amplitudes and lifetime at any time, respectively. The received TRPL decay curves for CoO and PC-fresh are shown in Fig. 5b. The fitted parameters and the obtained average carrier lifetime (τ_{ave}) are summarized in the table of Fig. 5c. CoO and PC-fresh have different electronic structures and hence different light absorption behavior. TRPL was carried out at corresponding absorption/energy bangaps. The τ_{ave} of sole CoO sample is 6.57 ns which was measured at the wavelength of 585 nm, i.e. its E_g of 2.6 eV, while the τ_{ave} of PC-fresh composite taken at CoO component's bandgap 2.9 eV decreased to 5.35 ns. The reduced average carrier lifetime could be associated with the effective spatial charge separation and transfer (i.e. between h^+/VBM_{CoO} and e^-/CBM_{Co3O4}) across the Z-scheme junction of CoO-Co_3O_4 in PC-fresh [52–54]. Note here, as the 2.9 eV E_g is from the intrinsic CoO and still detectable in TRPL, this implies the holes from the defect-free surface areas of CoO particles still exist which may recombine with e^-/CBM_{Co3O4}.

The TRPL measurement was also performed for the carrier lifetime related to the defects which absorbed deep red light at ~ 1.8 eV, i.e. the E_g between CBM_{CoO} and DEL_{CoO} in Fig. 5a. Impressively, the obtained τ_{ave} was further greatly reduced to 3.05 ns. The much quicker charge separation/transfer at ~1.8 eV from the defect states of CoO than that at ~ 2.9 eV from intrinsic CoO indicates that the radiative recombination between CBM_{CoO} and DEL_{CoO} is much better suppressed than that between CBM_{CoO} and VBM_{CoO}. This implies the emergence of much quicker non-radiative pathways via defects, rather than via the Z-scheme junction. When these pathways are connected to the oxygen vacancy (V_O) sites of CoO-(110) surface, the trapped electrons will favorably synergistically reduce the readily adsorbed N_2 to N-NH and the following NRR steps will have a lower barrier (Fig. 4d). This further verifies the main role of the active defects in CoO for NRR.

4. Conclusion

In this research, RGO templated 2D mixed-oxide (CoO and Co_3O_4) composites were synthesized through a simple and facile route at room temperature, with the ultra-small size of ~ 2–8 nm, much smaller than template-free CoO and Co_3O_4 particles with ~ 30–100 nm. Such diminutive CoO/Co_3O_4 composites possess great surface area (317 m^2 g^{-1}) and deep-red-light absorbing defect states, playing the role in

contamination-free N_2 photofixation under ambient conditions. Photo-activity from the composites is greatly enhanced compared with template-free single components of CoO and Co_3O_4. The unveiled CoO-Co_3O_4 Z-scheme heterojunction promotes nitrogen reduction at CoO surface, and oxygen oxidation reactions on Co_3O_4, respectively. Furthermore, the discovered photoreaction-induced cation oxidation (CoO to Co_3O_4) is readily recyclable by photo-reactivating the aged Co_3O_4 back to active CoO at room temperature, with NRR activity well maintained after six cycles of operation. All these room-temperature processes, from nanocatalyst synthesis, contamination-free redox reaction, to photoactivity reactivation, offer a facile way towards upscaling and practice, and hold great promise in achieving large scale applications for solar-driven zero-emission N_2 fixation.

CRediT authorship contribution statement

H.J. Lu, Y.M. Zhao and S.E. Saji contributed equally to this work. The conceptualization was proposed by Z.Y. Yin, and the main experiments were designed and carried out by H.J. Lu, S.E. Saji, and Z.Y. Yin. The characterizations on XPS and XANES were performed by X.M. Yin, A. Wibowo, C. S. Tang, S.B. Xi, and A. T.S. Wee. HRTEM, HAADF and ADF/EDS were done by P.F. Cao, M. Heggen, and R. E. Borkowski. The TRPL measurements were performed by A. Wibowo, M. Tebyetekerwa and H. T. Nguyen. The surface areas of catalysts were measured by B.R. Liu, and A. Tricoli. All theoretical calculations were done by Y.M. Zhao, and Q.B. Yan. Major supervision was undertaken by Z.Y. Yin, Q.B. Yan, and P.F. Cao. The original draft was written and edited by H.J. Lu, Y.M. Zhao, S.E Saji and Z.Y. Yin. All authors proof-read the manuscript.

Declaration of Competing Interest

The authors declare that they have no known competing financial interests or personal relationships that could have appeared to influence the work reported in this paper.

Acknowledgements

Appendix A. Supporting information

Supplementary data associated with this article can be found in the online version at doi:10.1016/j.apcatb.2021.121001.

References

[1] W.B. Qiu, X.Y. Xie, J.D. Qiu, W.H. Fang, R.P. Liang, X. Ren, X.Q. Ji, G.W. Cui, A. M. Asiri, G.L. Cui, B. Tang, X.P. Sun, High-performance artificial nitrogen fixation at ambient conditions using a metal-free electrocatalyst, Nat. Commun. 9 (2018) 3485.

[2] S.Y. Wang, F. Ichihara, H. Pang, H. Chen, J.H. Ye, Nitrogen fixation reaction derived from nanostructured catalytic materials, Adv. Funct. Mater. 28 (2018), 1803309.

[3] C. Tang, S.Z. Qiao, How to explore ambient electrocatalytic nitrogen reduction reliably and insightfully, Chem. Soc. Rev. 48 (2019) 3166–3180.

[4] X.Z. Chen, N. Li, Z.Z. Kong, W.J. Ong, X.J. Zhao, Photocatalytic fixation of nitrogen to ammonia: state-of-the-art advancements and future prospects, Mater. Horiz. 5 (2018) 9–27.

[5] Z.Y. Lu, S.E. Saji, J. Langley, Y.X. Lin, Z.R. Xie, K. Yang, L. Bao, Y.Y. Sun, S. B. Zhang, Y.H. Ng, L. Song, N. Cox, Z.Y. Yin, Selective N_2/H_2O adsorption onto 2D amphiphilic amorphous photocatalysts for ambient gas-phase nitrogen fixation, Appl. Catal. B Environ. (2021), 120240.

[6] Y. Liu, Z. Zhang, Y. Fang, B. Liu, J. Huang, F. Miao, Y. Bao, B. Dong, IR-Driven strong plasmonic-coupling on Ag nanorices/$W_{18}O_{49}$ nanowires heterostructures for photo/thermal synergistic enhancement of H_2 evolution from ammonia borane, Appl. Catal. B Environ. 252 (2019) 164–173.

[7] R. Shen, K. He, A. Zhang, N. Li, Y.H. Ng, P. Zhang, J. Hu, X. Li, In-situ construction of metallic $Ni_3C@Ni$ core–shell cocatalysts over g-C_3N_4 nanosheets for shell-thickness-dependent photocatalytic H2 production, Appl. Catal. B Environ. 291 (2021), 120104.

[8] X. Jing, N. Lu, J. Huang, P. Zhang, Z. Zhang, One-step hydrothermal synthesis of S-defect-controlled $ZnIn_2S_4$ microflowers with improved kinetics process of charge-carriers for photocatalytic H_2 evolution, J. Energy Chem. 58 (2021) 397–407.

[9] A.D. Allen, C.V. Senoff, Nitrogenopentammineruthenium(II) complexes, Chem. Commun. (1965) 621–622.

[10] B.A. MacKay, M.D. Fryzuk, Dinitrogen coordination chemistry: on the biomimetic borderlands, Chem. Rev. 104 (2004) 385–402.

[11] R.J. Burford, M.D. Fryzuk, Examining the relationship between coordination mode and reactivity of dinitrogen, Nat. Rev. Chem. 1 (2017) 0026.

[12] M.A. Legare, G. Belanger-Chabot, R.D. Dewhurst, E. Welz, I. Krummenacher, B. Engels, H. Braunschweig, Nitrogen fixation and reduction at boron, Science 359 (2018) 896–899.

[13] B.K. Sovacool, S.H. Ali, M. Bazilian, B. Radley, B. Nemery, J. Okatz, D. Mulvaney, Sustainable minerals and metals for a low-carbon future, Science 367 (2020) 30–33.

[14] T. Fan, L.G. Dou, H. Zhang, Nonprecious mixed oxide catalysts Co_3AlO and Co_2NiAlO derived from nanoflowerlike cobalt-based hydrotalcites for highly efficient oxidation of nitric oxide, RSC Adv. 6 (2016) 110274–110287.

[15] D.M. Hood, R.A. Johnson, A.E. Carpenter, J.M. Younker, D.J. Vinyard, G. G. Stanley, Highly active cationic cobalt(II) hydroformylation catalysts, Science 367 (2020) 542–548.

[16] S.Y. Reece, J.A. Hamel, K. Sung, T.D. Jarvi, A.J. Esswein, J.J.H. Pijpers, D. G. Nocera, Wireless solar water splitting using silicon-based semiconductors and earth-abundant catalysts, Science 334 (2011) 645–648.

[17] L.B. Liao, Q.H. Zhang, Z.H. Su, Z.Z. Zhao, Y.N. Wang, Y. Li, X.X. Lu, D.G. Wei, G. Y. Feng, Q.K. Yu, X.J. Cai, J.M. Zhao, Z.F. Ren, H. Fang, F. Robles-Hernandez, S. Baldelli, J.M. Bao, Efficient solar water-splitting using a nanocrystalline CoO photocatalyst, Nat. Nanotechnol. 9 (2014) 69–73.

[18] K. Chu, Y.P. Liu, Y.B. Li, H. Zhang, Y. Tian, Efficient electrocatalytic N_2 reduction on CoO quantum dots, J. Mater. Chem. A 7 (2019) 4389–4394.

[19] W.L. Shi, F. Guo, H.B. Wang, S.J. Guo, H. Li, Y.J. Zhou, C. Zhu, Y.H. Liu, H. Huang, B.D. Mao, Y. Liu, Z.H. Kang, New insight of water-splitting photocatalyst: H_2O_2-resistance poisoning and photothermal deactivation in sub-micrometer CoO octahedrons, ACS Appl. Mater. Interfaces 9 (2017) 20585–20593.

[20] W.L. Shi, F. Guo, C. Zhu, H.B. Wang, H. Li, H. Huang, Y. Liu, Z.H. Kang, Carbon dots anchored on octahedral CoO as a stable visible-light-responsive composite photocatalyst for overall water splitting, J. Mater. Chem. A 5 (2017) 19800–19807.

[21] T.T. Hong, Z.F. Liu, X.R. Zheng, J. Zhang, L. Yan, Efficient photoelectrochemical water splitting over Co_3O_4 and Co_3O_4/Ag composite structure, Appl. Catal. B Environ. 202 (2017) 454–459.

[22] S.X. Nie, R. Zhang, W.X. Lv, F.Y. Kong, W. Wang, Controlled synthesis of Co_3O_4 electrocatalysts with different morphologies and their application for oxygen evolution reaction, Int J. Electrochem. Sci. 13 (2018) 3843–3854.

[23] C. Zhu, M.M. Zhu, Y. Sun, Y.J. Zhou, J. Gao, H. Huang, Y. Liu, Z.H. Kang, Carbon-supported oxygen vacancy-rich Co_3O_4 for robust photocatalytic H2O2 production via coupled water oxidation and oxygen reduction reaction, ACS Appl. Energ. Mater. 2 (2019) 8737–8746.

[24] M.I. Ahmed, S. Chen, W.H. Ren, X.J. Chen, C. Zhao, Synergistic bimetallic $CoFe_2O_4$ clusters supported on graphene for ambient electrocatalytic reduction of nitrogen to ammonia, Chem. Commun. 55 (2019) 12184–12187.

[25] Q. Shen, Z.F. Chen, X.F. Huang, M.C. Liu, G.H. Zhao, High-yield and selective photoelectrocatalytic reduction of CO_2 to formate by metallic copper decorated Co3O4 nanotube arrays, Environ. Sci. Technol. 49 (2015) 5828–5835.

[26] D. Zhu, L.H. Zhang, R.E. Ruther, R.J. Hamers, Photo-illuminated diamond as a solid-state source of solvated electrons in water for nitrogen reduction, Nat. Mater. 12 (2013) 836–841.

[27] S.E. Saji, H.J. Lu, Z.Y. Lu, A. Carroll, Z.Y. Yin, An experimentally verified LC-MS protocol towards an economical, reliable and quantitative isotopic analysis in nitrogen reduction reactions, Small Methods (2021), 2000694.

[28] G. Kresse, J. Furthmüller, Efficient iterative schemes for Ab initio total-energy calculations using a plane-wave basis set, Phys. Rev. B 54 (1996) 11169.

[29] P.E. Blöchl, Projector augmented-wave method, Phys. Rev. B 50 (1994) 17953–17979.

[30] J.P. Perdew, K. Burke, M. Ernzerhof, Generalized gradient approximation made simple, Phys. Rev. Lett. 77 (1996) 3865–3868.

[31] T. Ling, D.-Y. Yan, Y. Jiao, H. Wang, Y. Zheng, X. Zheng, J. Mao, X.-W. Du, Z. Hu, M. Jaroniec, S.-Z. Qiao, Engineering surface atomic structure of single-crystal cobalt (II) oxide nanorods for superior electrocatalysis, Nat. Commun. 7 (2016) 12876.

[32] S. Grimme, J. Antony, S. Ehrlich, H. Krieg, A consistent and accurate ab initio parametrization of density functional dispersion correction (DFT-D) for the 94 elements H-Pu, J. Chem. Phys. 132 (2010) 154104.

[33] C. Liu, Q. Li, C. Wu, J. Zhang, Y. Jin, D.R. MacFarlane, C. Sun, Single-boron catalysts for nitrogen reduction reaction, J. Am. Chem. Soc. 141 (2019) 2884–2888.

[34] H.J. Wu, G.L. Wu, Y.Y. Ren, L. Yang, L.D. Wang, X.H. Li, Co^{2+}/Co^{3+} ratio dependence of electromagnetic wave absorption in hierarchical $NiCo_2O_4$-$CoNiO_2$ hybrids, J. Mater. Chem. C 3 (2015) 7677–7690.

[35] Y. Sun, J. Liu, N. Yang, Y. Zhu, One-dimensional heterostructured palladium oxide-cobalt oxide catalyst for the catalytic oxidation of methane, Chemcatchem 9 (2017) 738–745.

[36] X.Y. Yu, Q.Q. Meng, T. Luo, Y. Jia, B. Sun, Q.X. Li, J.H. Liu, X.J. Huang, Facet-dependent electrochemical properties of Co_3O_4 nanocrystals toward heavy metal ions, Sci. Rep. 3 (2013).

[37] Z.H. Zhen, Z.Q. Jiang, X.N. Tian, L.S. Zhou, B.L. Deng, B.H. Chen, Z.J. Jiang, Core@shell structured Co-CoO@NC nanoparticles supported on nitrogen doped carbon with high catalytic activity for oxygen reduction reaction, RSC Adv. 8 (2018) 14462–14472.

[38] H.J. Shin, K.K. Kim, A. Benayad, S.M. Yoon, H.K. Park, I.S. Jung, M.H. Jin, H. K. Jeong, J.M. Kim, J.Y. Choi, Y.H. Lee, Efficient reduction of graphite oxide by sodium borohydride and its effect on electrical conductance, Adv. Funct. Mater. 19 (2009) 1987–1992.

[39] Z.Y. Lin, C. Du, B. Yan, G.W. Yang, Two-dimensional amorphous CoO photocatalyst for efficient overall water splitting with high stability, J. Catal. 372 (2019) 299–310.

[40] S.Z. Andersen, V. Colic, S. Yang, J.A. Schwalbe, A.C. Nielander, J.M. McEnaney, K. Enemark-Rasmussen, J.G. Baker, A.R. Singh, B.A. Rohr, M.J. Statt, S.J. Blair, S. Mezzavilla, J. Kibsgaard, P.C.K. Vesborg, M. Cargnello, S.F. Bent, T.F. Jaramillo, I.E.L. Stephens, J.K. Norskov, I. Chorkendorff, A rigorous electrochemical ammonia synthesis protocol with quantitative isotope measurements, Nature 570 (2019) 504–508.

[41] H. Hirakawa, M. Hashimoto, Y. Shiraishi, T. Hirai, Photocatalytic conversion of nitrogen to ammonia with water on surface oxygen vacancies of titanium dioxide, J. Am. Chem. Soc. 139 (2017) 10929–10936.

[42] K. Gelderman, L. Lee, S.W. Donne, Flat-band potential of a semiconductor: using the Mott-Schottky equation, J. Chem. Educ. 84 (2007) 685–688.

[43] L. Liao, Q. Zhang, Z. Su, Z. Zhao, Y. Wang, Y. Li, X. Lu, D. Wei, G. Feng, Q. Yu, X. Cai, J. Zhao, Z. Ren, H. Fang, F. Robles-Hernandez, S. Baldelli, J. Bao, Efficient solar water-splitting using a nanocrystalline CoO photocatalyst, Nat. Nanotechnol. 9 (2014) 69–73.

[44] A.U. Mane, S.A. Shivashankar, MOCVD of cobalt oxide thin films: dependence of growth, microstructure, and optical properties on the source of oxidation, J. Cryst. Growth 254 (2003) 368–377.

[45] C. Ravi Dhas, R. Venkatesh, K. Jothivenkatachalam, A. Nithya, B. Suji Benjamin, A. Moses Ezhil Raj, K. Jeyadheepan, C. Sanjeeviraja, Visible light driven photocatalytic degradation of Rhodamine B and Direct Red using cobalt oxide nanoparticles, Ceram. Int. 41 (2015) 9301–9313.

[46] Q. Xu, L. Zhang, J. Yu, S. Wageh, A.A. Al-Ghamdi, M. Jaroniec, Direct Z-scheme photocatalysts: principles, synthesis, and applications, Mater. Today 21 (2018) 1042–1063.

[47] J. Yuan, X. Yi, Y. Tang, M. Liu, C. Liu, Efficient photocatalytic nitrogen fixation: enhanced polarization, activation, and cleavage by asymmetrical electron donation to N≡N bond, Adv. Funct. Mater. 30 (2020), 1906983.

[48] W. Guo, K. Zhang, Z. Liang, R. Zou, Q. Xu, Electrochemical nitrogen fixation and utilization: theories, advanced catalyst materials and system design, Chem. Soc. Rev. 48 (2019) 5658–5716.

[49] X. Lv, W. Wei, F. Li, B. Huang, Y. Dai, Metal-free B@g-CN: visible/infrared light-driven single atom photocatalyst enables spontaneous dinitrogen reduction to ammonia, Nano Lett. 19 (2019) 6391–6399.

[50] J. Zhao, Z. Chen, Single Mo atom supported on defective boron nitride monolayer as an efficient electrocatalyst for nitrogen fixation: a computational study, J. Am. Chem. Soc. 139 (2017) 12480–12487.

[51] W. Zhao, L. Zhang, Q. Luo, Z. Hu, W. Zhang, S. Smith, J. Yang, Single $Mo_1(Cr_1)$ atom on nitrogen-doped graphene enables highly selective electroreduction of nitrogen into ammonia, ACS Catal. 9 (2019) 3419–3425.

[52] Z. Zhang, J. Huang, M. Zhang, Q. Yuan, B. Dong, Ultrathin hexagonal SnS_2 nanosheets coupled with g-C_3N_4 nanosheets as 2D/2D heterojunction photocatalysts toward high photocatalytic activity, Appl. Catal. B Environ. 163 (2015) 298–305.

[53] M.-Z. Ge, C.-Y. Cao, S.-H. Li, Y.-X. Tang, L.-N. Wang, N. Qi, J.-Y. Huang, K.-Q. Zhang, S.S. Al-Deyab, Y.-K. Lai, In situ plasmonic Ag nanoparticle anchored TiO_2 nanotube arrays as visible-light-driven photocatalysts for enhanced water splitting, Nanoscale 8 (2016) 5226–5234.

[54] C. Li, Y. Du, D. Wang, S. Yin, W. Tu, Z. Chen, M. Kraft, G. Chen, R. Xu, Unique P—Co—N surface bonding states constructed on g-C3N4 nanosheets for drastically enhanced photocatalytic activity of H_2 evolution, Adv. Funct. Mater. 27 (2017), 1604328.